Cite this: *Nanoscale*, 2011, **3**, 5076

www.rsc.org/nanoscale

PAPER

Structural transformation of tungsten oxide nanourchins into IF–WS_2 nanoparticles: an aberration corrected STEM study†

Francis Leonard-Deepak,[ab] Carlos Fernando Castro-Guerrero,[a] Sergio Mejía-Rosales[c] and Miguel José-Yacamán*[a]

Received 18th July 2011, Accepted 22nd September 2011
DOI: 10.1039/c1nr10862j

IF–WS_2 nanoparticles synthesized starting from tungsten oxide nanourchins have been investigated by using aberration corrected scanning transmission electron microscopy (C_s-STEM). The synthesis process produced IF–WS_2 nanoparticles of two different and well differentiated ranges of size. High resolution HAADF–STEM images and their comparison with simulated STEM micrographs reveal the predominance of stacking of the type 1T close to the border of the structure; the observation of this kind of stacking, observed previously in IF–MoS_2 but never reported before in the case of the IF–WS_2 nanostructures, adds a new dimension to the existing understanding of structure and stacking in the case of the nanostructures of transition metal chalcogenides.

1. Introduction

Ever since the discovery that closed-cage structures of inorganic compounds (such as WS_2 and MoS_2), commonly known by the generic names of *inorganic fullerenes* (IFs) and *inorganic nanotubes* (INTs), are formed by a structure similar to those of carbon, there has been tremendous progress in this area of research.[1] Although the first synthesis attempts yielded only a few milligrams of the IF–WS_2, thereafter, bulk synthesis of inorganic fullerenes of MS_2 (M = Mo, W) from their respective trioxides was carried out and their reaction mechanism was elucidated in great detail subsequently.[2] This was an important step towards the establishment of inorganic fullerenes and nanotubes as a promising kind of structures, since now with the scale-up of synthesis new applications could be envisaged.[3] Thus, IF–WS_2 nanoparticles were used in coating of different NiTi substrates by the electrodeposition procedure for friction reduction properties, and their friction tests presented up to 66% reduction of the friction coefficient.[4] IF–WS_2 nanoparticles were also shown to increase the fracture toughness significantly in epoxy systems at very low concentrations while increasing its storage modulus and preserving its glass transition temperature.[5,6] The non-reactive and reactive adsorption of thiophene on the IF–WS_2 nanoparticles revealed catalytic activity for the hydrodesulfurization (HDS) process.[7] Interesting studies have also been carried out in which the adsorption of Au nanoparticles (NPs) to the surface of IF–WS_2 nanostructures was investigated; it was found that the Au NPs adhere to IF–WS_2 reactive sites in such a way that the Au NPs were used as probes to localize surface defects in the IF–WS_2 nanoparticles.[8] Surface-modified IF–WS_2 nanoparticles have been shown to display improved dispersion in oil-based suspensions. Thus, the application of an alkyl-silane coating reduces the tendency of the IF–WS_2 nanoparticles to agglomerate and consequently improves the long-term tribological behavior of oil formulated with the IF additive.[9] Thus with unraveling new properties and applications initiated by the IF–WS_2, there has been a large amount of interest generated by this area of research. New methods of synthesis and investigations of various properties of the IF–WS_2 are being carried out with great interest. These methods of synthesis include the reaction of sulfur powder (S) and as-prepared WO_3 nanoparticles in a hydrogen atmosphere at a heating temperature of 500–650 °C.[10,11] Hollow and filled IF–WS_2 nanoparticles have been obtained *via* metal–organic chemical vapor deposition (MOCVD).[12,13] In a related synthesis, IF–WS_2 nanoparticles were obtained by the vapor-phase synthesis of WCl_n and H_2S.[14] Other methods of synthesis include atmospheric chemical vapor deposition (APCVD), starting from solid precursors.[15,16] In this context it must also be mentioned the synthesis of new hybrid structures like the inorganic *nanobuds*: WS_2 nanotubes decorated with fullerene-like particles synthesized by the sulfurization of W_5O_{14} nanowires.[17] However, what seemed to be lacking so far is the in-depth structural investigation of the IF–WS_2 nanoparticles themselves. This was accomplished recently in a study based on the use of electron tomography imaging, where it was possible to

[a]*Department of Physics and Astronomy, University of Texas at San Antonio, One UTSA Circle, San Antonio, Texas, 78249, USA. E-mail: miguel.yacaman@utsa.edu; Fax: +1 210 458 4919; Tel: +1 210 458-5451*
[b]*International Iberian Nanotechnology Laboratory, Avda Mestre Jose Veiga, Braga, 4715, Portugal*
[c]*Center for Innovation and Research in Engineering and Technology, CICFIM-Facultad de Ciencias Físico-Matemáticas, Universidad Autónoma de Nuevo León, San Nicolás de los Garza, NL, 66450, México*
† Electronic supplementary information (ESI) available: Raman spectra of the WO_x–$W_{18}O_{49}$ nanourchins, XRD pattern, EDAX spectrum and elemental maps of the IF–WS_2 nanoparticles. See DOI: 10.1039/c1nr10862j

achieve a reliable reconstruction of the 3D structure of nested IF–WS_2 with sub-nanometre resolution using electron microscopes that are not aberration-corrected. Model-based simulations were also used to identify the appropriate imaging parameters under which structural features such as the shell structure can be retained in the tomogram reconstructed from bright-field micrographs.[18]

We report the results of extensive investigations on the IF–WS_2 nanoparticles synthesized starting from the tungsten oxide nanourchins, using aberration corrected (C_s) STEM to identify the atomic structure in great detail. It is hoped that such a study will shed new information on the structure, stacking and growth mechanism of IF–WS_2 nanoparticles, with the aim of using these structures as solid lubricants, as composites, and as active agents in catalysis. To our knowledge, this study is the first of its type for the specific case of IF–WS_2 nanoparticles.

2. Experimental section

2.1 Synthesis

WO_x–$W_{18}O_{49}$ nanourchins. A mix of approximately 0.4807 g tungsten hexacarbonyl $W(CO)_6$ and 10 mL ethanol was kept in an autoclave for 12 hours at a temperature of 200 °C. At the end of the reaction, the products (blue powder/clear crystals) were washed with acetone and kept in an oven to obtain the final dried powder product. Other reactions were carried out by varying the amount of $W(CO)_6$ and ethanol (1.996 g $W(CO)_6$ and 80 mL ethanol, and 1.25 g $W(CO)_6$ and 80 mL ethanol), and the reaction time (12 h and 24 h) to obtain the desired products.

IF–WS_2 nanoparticles

(i) Using sulfur powder. 0.2201 g of the WO_x–$W_{18}O_{49}$ sample and 0.0931 g of sulfur (Sigma-Aldrich, 99.98%) were ground together for 1 h. The amount of sulfur was increased to five times the original quantity, in order to ensure that the mix contained sulfur in excess, and afterwards the sample was put into a crucible and placed in the hot zone of a tube furnace. This mixture was heated at 900 °C/1000 °C for 30 minutes under an atmosphere of nitrogen. After the reaction the tube furnace was allowed to cool down to room temperature, and the resulting black powder was collected for further analysis.

(ii) Using thiourea. About 0.1 g of the WO_x–$W_{18}O_{49}$ sample was ground with 0.1004 g of thiourea (Sigma-Aldrich, ≥99%) for 1 h. Approximately five times the weight of thiourea was added to the mixture (to ensure that the thiourea was in excess), and put into a crucible which was placed in the hot zone of a tube furnace. This mixture was heated at 900 °C/1000 °C for 30 minutes under an atmosphere of nitrogen. After the reaction the tube furnace was allowed to cool down to room temperature, and the resulting black powder was collected.

2.2 Characterization

The oxide and the sulfide samples were analyzed by X-ray diffraction (XRD) using a Rigaku Ultima IV X-ray diffractometer. For the electron microscopy analysis, the sample was dispersed in ethanol and a drop of this suspension was deposited onto a holey carbon microgrid. The samples were characterized using a Hitachi S-5500 scanning electron microscope (SEM) with a bright-field/dark-field (BF/DF) duo STEM detector. SEM-EDAX (Energy Dispersive X-ray Analysis) spectroscopy as well the corresponding chemical elemental maps were obtained using a Brucker-EDX instrument in the SEM. A JEOL JEM-2010F (FEG-TEM) operated at 200 kV with a 0.1 nm lattice resolution was employed to record high resolution transmission electron microscopy (HRTEM) images and electron diffraction (ED) patterns, and to perform the EDX analysis of the materials. For the aberration (C_s) corrected characterization, the samples were analyzed by scanning transmission electron microscopy (STEM) using a JEOL ARM (200F) 200 kV FEG-STEM/TEM equipped with a CEOS C_s corrector on the illumination system. The probe size used for acquiring the HAADF as well as the BF-STEM images was 9C (23.2 pA) and the CL aperture size was 40 μm. High angle annular dark-field (HAADF) STEM images were acquired with a camera length of 8 cm/6 cm and the collection angle of 68–280 mrad/90–270 mrad. The BF-STEM images were obtained using a 3 mm/1 mm aperture and a collection angle of 17 mrad/5.6 mrad was used (camera length in this case was 8 cm). The HAADF as well as the BF images were acquired using a digiscan camera. In order to reduce the noise of the images and to obtain clearer images the raw data were filtered using the Richardson–Lucy algorithm implemented by Ishizuka.[19] The EDS analysis was performed using EDAX instrumentation attached to the JEOL-ARM microscope. Spectra, line scans, and chemical maps for the various elements were obtained using the EDAX genesis software. For the EDS analysis the probe size used was 6 C (145 pA) and the CL aperture size was 40 μm. To obtain the Raman spectrum, a high resolution confocal microscope (HORIBA Jobin Yvon) was used with a source of monochromatic radiation of 785 nm. For Raman measurements a 10× objective and a laser power of 3 mw were used and the signal detection is achieved through the use of a sensitive charge coupled device (CCD) array detector. Molecular models of the structures were prepared using the Materials Studio Visualizer software[20] and (HAADF) STEM simulated images of the models were calculated using the STEM module of the *x*HREM program by Ishizuka, based on the FFT multislice method.[21] The simulated micrographs were compared against the corresponding real STEM images, and following the results of the comparisons, the models were refined and a new set of simulated images was calculated. This simulation process was repeated until a fair agreement between simulated and real images was obtained.

3. Results and discussion

Fig. 1a shows the SEM image of the large arrays of nanourchins obtained by the reaction of $W(CO)_6$ and ethanol. A closer look at the nanourchins is provided in the SEM images of Fig. 1b and c, wherein it can be seen that the nanourchins consist of a central core with short spiky nanorod-like branches emanating from all around the core. The typical diameter of the core of the nanourchins is about 500 nm. The central core is found to be largely spherical, although some irregular shapes have also been observed. Shown in the inset of Fig. 1a is the photograph of the marine species, the sea-urchin. The presence of the characteristic elements of W and O that make up the nanourchins was

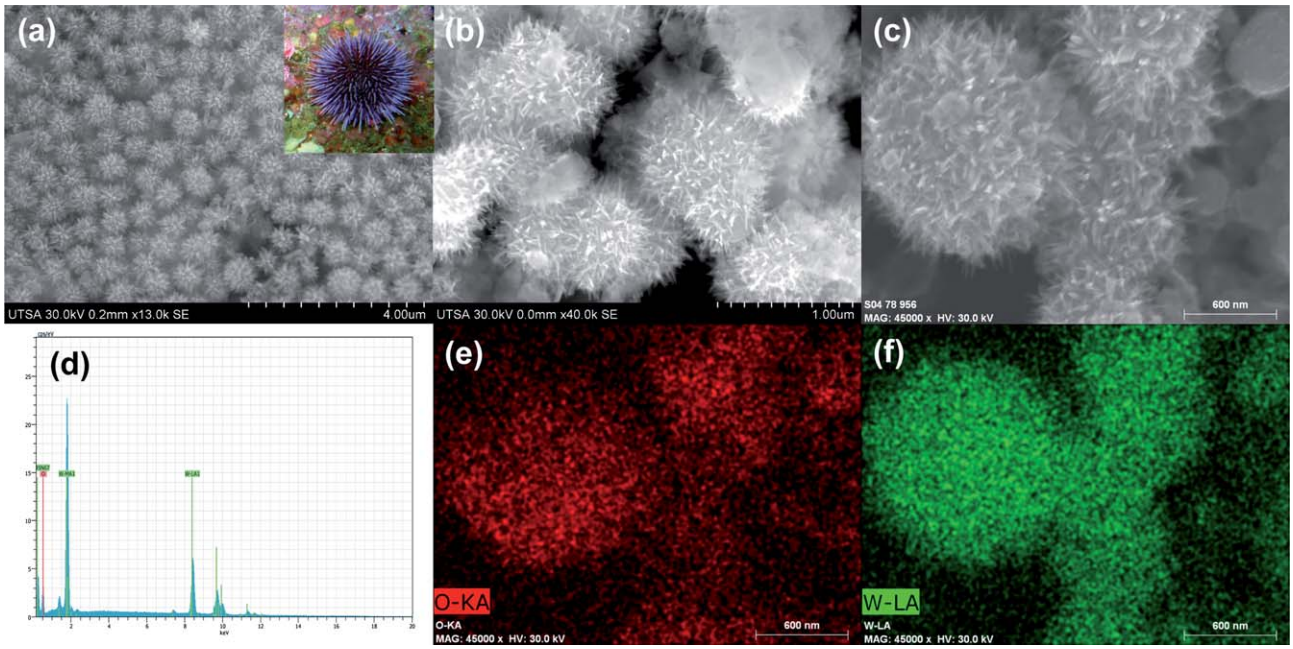

Fig. 1 (a) Low magnification and (b), (c) high magnification SEM images of the large arrays of nanourchins obtained by the reaction of $W(CO)_6$ and ethanol; inset of (a) is the photograph of the marine species, the sea-urchin, (d) and (e), (f) EDAX spectrum and the corresponding elemental maps of the nanourchins.

confirmed by the results of the SEM-EDAX analysis. Shown in Fig. 1d is the EDAX spectrum of the nanourchins showing the characteristic W(L,M) and the O(K) lines. The corresponding elemental maps are shown in Fig. 1e and Fig. 1f (OK and WL maps of the nanourchins). A closer look at the nanourchins is provided by the TEM images shown in Fig. 2. Fig. 2a and b reveal the core and the emanating nanorods from the core of the nanourchins more clearly. The nanorods project outward from the core of the nanourchins in all directions. The length of the nanorods is about ~100 nm, whereas the diameter of the nanorods is ~5 nm showing that the nanorods have a huge aspect ratio. Fig. 2c and d show the HRTEM images of the nanorods revealing their single-crystalline nature. The nanorods have a lattice spacing of 0.377 nm, corresponding to the (010) planes

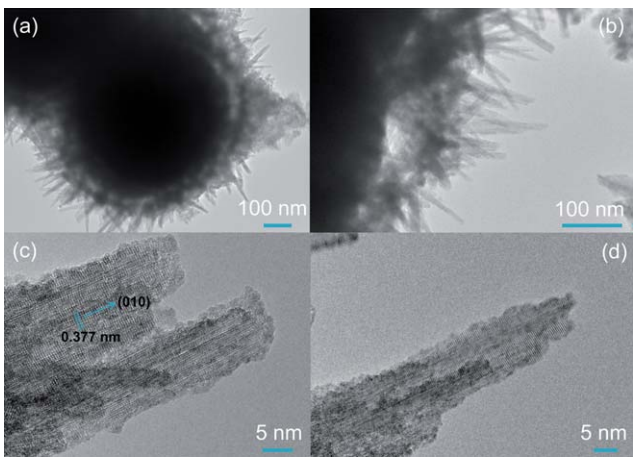

Fig. 2 (a and b) Low magnification TEM images of the nanourchins, (c) and (d) HRTEM images of the nanorods emanating from the core.

of the monoclinic $W_{18}O_{49}$ (JCPDS card: 05-0392). The nanorods are sensitive to the electron beam, as can be seen in the images from their deterioration/recrystallization around the edges, which progresses very rapidly to the entire nanorod. X-Ray diffraction (XRD) of the nanourchins indicates that the products consist of two different phases. One of the phases can be indexed with the peaks matching closely to that of the monoclinic $W_{18}O_{49}$ (JCPDS card: 05-0392) phase (the nanorods that emanate from the nanourchins as also confirmed by HRTEM); however, the second phase, which is presumably the core of the nanourchins, although very close, cannot be fully matched with that of the monoclinic WO_2 (JCPDS card: 86-0134) and hence this phase is designated as WO_x.[22] The TEM and XRD results indicate that the nanourchins are composed of WO_x spheres and $W_{18}O_{49}$ nanorods in the core and shell structures, respectively. The Raman spectrum of the WO_x–$W_{18}O_{49}$ nanourchins show four well-resolved peaks at 254, 324, 699 and 798 cm^{-1} (see ESI, Fig. S1†).[22]

Shown in Fig. 3 are the TEM and HRTEM images of the IF–WS_2 nanoparticles obtained by the reaction of the WO_x–$W_{18}O_{49}$ nanourchin sample with S powder synthesized at 900 °C. Large yields of IF–WS_2 nanoparticles were obtained at this temperature of synthesis. Fig. 3a–c show IF–WS_2 nanoparticles having a diameter of ~300 to 400 nm. A closer look at these nanoparticles (Fig. 3b and c) reveals the presence of the hollow core (Fig. 3b) and the hair-like outgrowths (Fig. 3c) on the surface of each of these individual nanoparticles. These hair-like outgrowths correspond to the incomplete layers of WS_2 that have not provided the complete closure of the WS_2 nanoparticle. In contrast to the large diameter IF–WS_2 nanoparticles, Fig. 3d–f show the presence of nanoparticles with smaller diameter (~50 to 100 nm). A closer look at the smaller nanoparticles is provided by the HRTEM images shown in Fig. 3e and f. The hollow empty

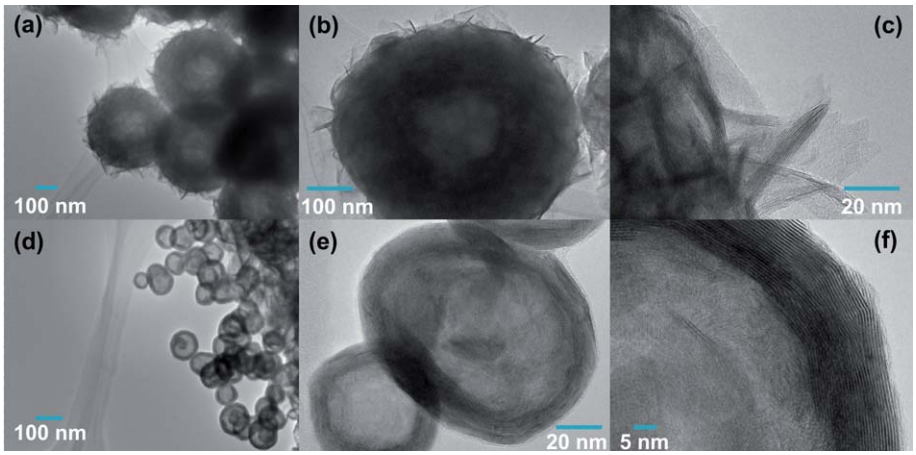

Fig. 3 (a–c) TEM and HRTEM images of the large diameter IF–WS_2 nanoparticles, (d–f) TEM and HRTEM images of the smaller diameter IF–WS_2 nanoparticles (using S powder).

core in the nanoparticles as well as the number of layers (~25 layers) are clearly evident from these images. The presence of the characteristic elements of W and S in the atomic ratio of 1 : 2 has been identified by EDAX. In addition, the elemental maps have also revealed the presence of W and S (see ESI, Fig. S3 and 4†). The difference in diameter of the IF–WS_2 nanoparticles arises from the different sulfidized products, namely the core (WO_x) and the nanorods projecting outward from the core ($W_{18}O_{49}$ nanorods), in the course of formation of the IF–WS_2 nanoparticles (Fig. 8). Thus, this difference in diameter is clearly related to the different sulfidized products. Although we have carried out reactions at 1000 °C, the best temperature of synthesis that yields large amounts of IF–WS_2 is 900 °C.

In contrast to the reaction using S powder, the reaction of thiourea with the oxide nanourchins (900 °C) produced IF–WS_2 nanoparticles with smaller diameter. Here again there are IF–WS_2 nanoparticles of two different diameters (~100 nm and ~20 nm). Fig. 4a shows several IF–WS_2 nanoparticles with the larger diameter, whereas Fig. 4b shows IF–WS_2 nanoparticles with the smaller diameter (~20 nm). A closer look at the small diameter IF–WS_2 nanoparticles is provided by the HRTEM images in Fig. 4c and d. The images reveal the following features: (i) the number of layers is ~15 and (ii) the nanoparticles are well faceted. Interestingly, the layers have complete closure in the case of the reaction of the nanourchins with thiourea, unlike the case of the particles produced by the reaction with S powder, where it was seen that due to the incomplete closure of the outermost layers, hair-like outgrowths were evident in the structure of the large-diameter IF–WS_2 nanoparticles.

We have used probe aberration corrected electron microscopy to gain insights into the structure, stacking of layers and their inherent features. Fig. 5a and b show the BF-STEM and the DF-STEM images of the IF–WS_2 nanoparticles (obtained by using

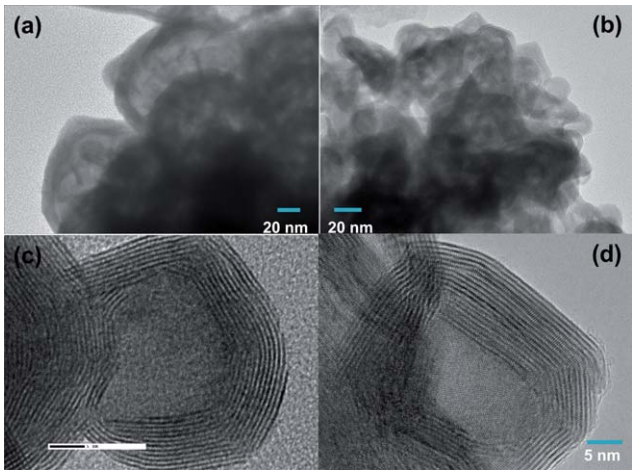

Fig. 4 (a) TEM image of the large diameter IF–WS_2 nanoparticles, (b–d) TEM and HRTEM images of the smaller diameter IF–WS_2 nanoparticles (using thiourea).

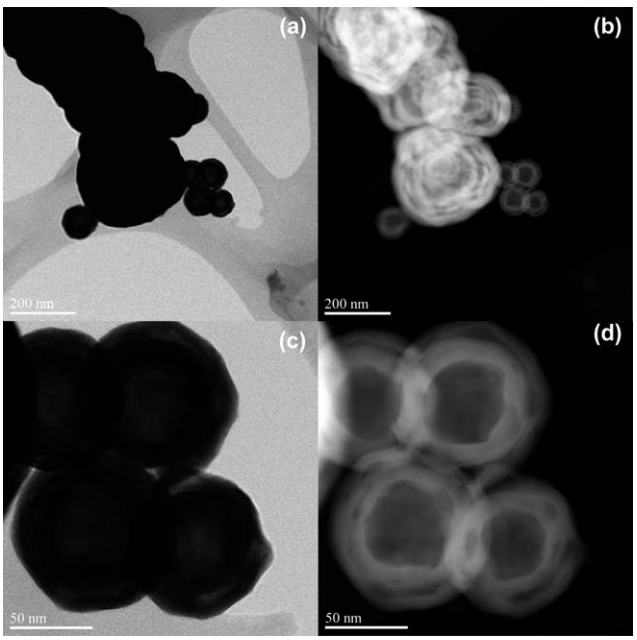

Fig. 5 (a–d) show the BF-STEM and the DF-STEM images of the IF–WS_2 nanoparticles (obtained by using S powder at the reaction temperature of 900 °C).

S powder at the reaction temperature of 900 °C). The images clearly show the presence of the large diameter and the small diameter IF–WS_2 nanoparticles in the vicinity of each other (see also Fig. 8). A closer look at the smaller diameter IF–WS_2 nanoparticles is provided in the BF-STEM and the DF-STEM images in Fig. 5c and d. The hollow core and the concentric layers that make up the nanoparticle are clearly evident in all these images. A closer look providing information on the number of layers (~15 layers in this case) that make up the nanoparticles is provided by the BF-STEM and the DF-STEM images in Fig. 6a and b. In addition to this, the presence of the high intensity spots presumably due to the position of the W atoms that make up the WS_2 chevron is also evident from Fig. 6b. A view of the W atoms (bright atom contrast) and the S atoms (which have a lesser intensity due to the difference in the Z number) can clearly help distinguish the S–W–S chevron that makes up the individual layers of the entire nanoparticles (Fig. 6c and d). Conventional high-resolution transmission electron microscopy (HRTEM), which has been used previously to study nanoparticles/nanowires/nanotubes, is a powerful tool.[23–25] However, it is far less capable than high-resolution scanning transmission electron microscopy (STEM) in identifying single atoms. The images generated by using the high-angle scattered electrons in STEM are incoherent, giving a contrast that is strongly dependent on the atomic number Z of the observed atom. This method is therefore the most effective technique available for detecting different Z atoms. Aberration correction allows sub-angstrom probes to be formed, which greatly improve the signal-to-noise ratio and sensitivity, and allow the resolution of single atoms.[26–28] Hence, sub-angstrom probes are crucial for imaging single atoms close to the surface of the structure. The variations on the HAADF contrast (Fig. 6b and d) cannot be explained on the basis of thickness changes. Therefore, most important contributions should originate from compositional variations, revealed by the difference in atomic number (Z) that exists among tungsten (atomic number = 74) and sulfur (atomic number = 16). The HAADF intensity is considered to be proportional to $Z^{1.7}$. It is well established that the projected atomic columns in HAADF–STEM images appear in bright contrast. Since the images are incoherent, no interference effects are produced between the Bloch waves that propagate through the crystal and thus the contrast strongly depends on the atomic number.[29–31]

There is an interesting observation that can be made by the close inspection of Fig. 6b and d: even with the availability of high resolution micrographs, the task of identifying the details of the WS_2 layers in the structure is not straightforward. In the first place, the large difference in atomic number between W and S makes that, in order to visualize the sulfur atoms on HAADF–STEM, the intensity due to the presence of tungsten becomes saturated; in second place, the 1T and prismatic phases are not as easily to contrast as in similar structures of MoS_2, since chevron-like motifs associated with layers correlated in a prismatic fashion are not as clearly formed as in the MoS_2 case, either in bright field or in dark field micrographs.[32–35] Nevertheless, the W positions are well defined in large regions of the HAADF–STEM micrographs, and taking these positions as reference, altogether with the inspection of the corresponding bright field images and the calculation of simulated HAADF–STEM micrographs, it is possible to build up a model that reproduces the main features of the WS_2 structure. This has been done in the construction of Fig. 7, where we have overlaid an atomistic model that explains the layer structure of the STEM micrograph. In the model, gray spheres represent W atoms, and yellow spheres represent S atoms. As we remarked on the figure, close to the border of the

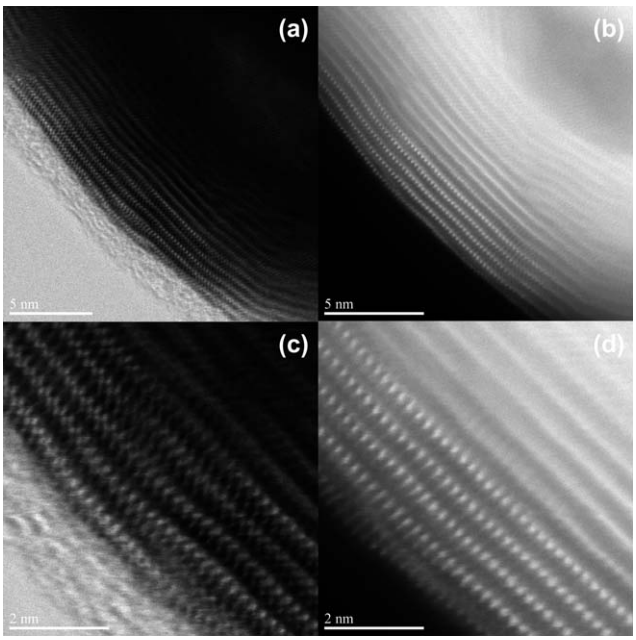

Fig. 6 (a–d) show the ultra-high resolution BF-STEM and the DF-STEM images of the IF–WS_2 nanoparticles. The bright atom contrast arises from the W atoms. The presence of the S atoms in the S–W–S chevron can be ascertained. The resolution and contrast are high enough to identify the W and S columns.

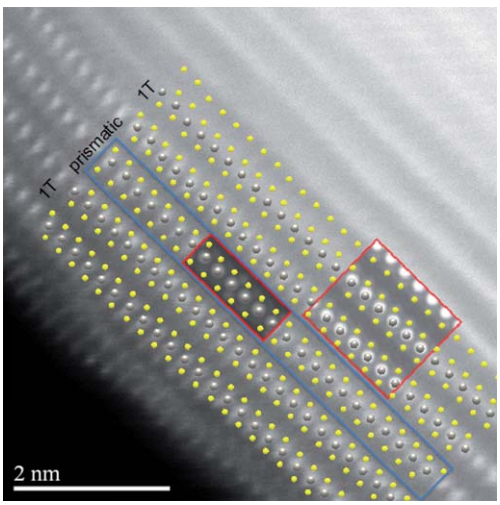

Fig. 7 High resolution HAADF–STEM micrograph of the row structure of WS_2, and an atomistic model that explains the sequencing of the rows. Gray spheres represent W atoms; yellow spheres represent S atoms. The row marked with a blue rectangle corresponds to a prismatic WS_2 row separating two regions with 1T arrangement. The red rectangles correspond to the superposition of HAADF–STEM simulated micrographs.

structure, the characteristic sequence of a 1T phase is lost by the appearance of a prismatic row (marked with a long blue rectangle). After this line, the row, the structure regains its 1T phase, but it is not possible to identify if this trend is kept by the most external row of the structure. We have also overlapped simulated STEM images (marked in red) corresponding to the prismatic and 1T arrangements. From the simulations we can note that the bright spots that mark the presence of sulfur are not as well defined as those due to W, something expected for atoms of low atomic number. The simulated images were obtained at 200 kV, using a simulated HAADF detector set at 50 mrad and 200 mrad as inner and outer angles, respectively. The overall intensity differences between the two simulated micrographs are merely incidental. We also tried to build up the opposite model (a 1T row separating two prismatic regions), but this alternative model failed to adequately match the atomic positions of tungsten, which made an even stronger argument favoring the model shown in Fig. 7. The tools used to investigate the kind of layering in the structure does not allow us to reach a conclusion on the layers far from the border of the particles, since the STEM signal due to the thickness of the atomic rows becomes saturated.

It has been shown recently that such an octahedrally coordinated phase (1T) can exist in the case of closed-cage nanoparticles (*e.g.* MoS_2 nanoparticles). This phase was predicted to be metallic, but is not stable in the bulk form.[34] In the case of WS_2, such a phase has been shown to exist possibly in exfoliated-restacked WS_2 layers and suggests a metallic nature to the material.[35]

An investigation on the stability of the 1T stacking of the WS_2 external layers from an energetic perspective is a pending issue that deserves close attention; a computational DFT study of the energy landscape of these structures, altogether with additional synthesis experiments under different conditions, will give elements to describe the specific details of the stacking, and will explain how dependent is the appearance of the 1T stacking on the specifics of the synthesis. Notwithstanding this pending work, we believe that the observation of such a phase for the first time in the present study has the potential of changing how the landscape of the transition metal chalcogenide nanoparticles and nanotubes is understood, and it would indeed be worthwhile to investigate the electronic properties of this new phase.

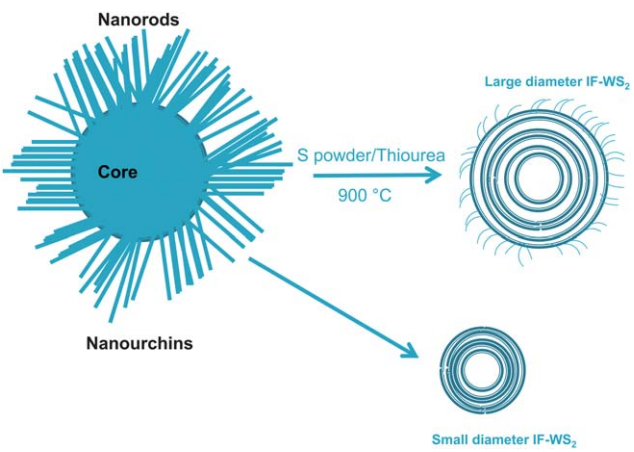

Fig. 8 Schematic showing the transformation process of the tungsten oxide nanourchins into the IF–WS_2 nanoparticles aided by the different sulfur sources (S powder and thiourea).

4. Conclusions

IF–WS_2 nanoparticles have been synthesized starting from tungsten oxide nanourchins, using two different sulfur sources, namely S powder and thiourea (Fig 8). Various conditions were investigated to identify the best yield of the IF–WS_2 nanoparticles. The nanoparticles obtained by this method may lie in one of two different ranges of diameter, depending on the starting oxide material. Using a combination of advanced electron microscopic techniques the local structure and stacking of the S–W–S chevron were carefully investigated. These studies revealed the presence of the octahedrally coordinated 1T type of phase which is unusual for these materials and has not been previously reported.

References

1 R. Tenne, L. Margulis, M. Genut and G. Hodes, *Nature*, 1992, **360**, 444–446.
2 Y. Feldman, G. L. Frey, M. Homyonfer, V. Lyakhovitskaya, L. Margulis, H. Cohen, G. Hodes, J. L. Hutchison and R. Tenne, *J. Am. Chem. Soc.*, 1996, **118**, 5362–5367.
3 Y. Feldman, A. Zak, R. Popovitz-Biro and R. Tenne, *Solid State Sci.*, 2000, **2**, 663–672.
4 G. R. Samorodnitzky-Naveh, M. Redlich, L. Rapoport, Y. Feldman and R. Tenne, *Nanomedicine*, 2009, **4**, 943–950.
5 A. Buchman, H. Dodiuk-Kenig, A. Dotan, R. Tenne and S. Kenig, *J. Adhes. Sci. Technol.*, 2009, **23**, 753–768.
6 M. Shneider, H. Dodiuk, S. Kenig and R. Tenne, *J. Adhes. Sci. Technol.*, 2010, **24**, 1083–1095.
7 J. Goering, U. Burghaus, B. W. Arey, O. Eidelman, A. Zak and R. Tenne, *Catal. Lett.*, 2008, **125**, 236–242.
8 C. Shahar, R. Levi, S. R. Cohen and R. Tenne, *J. Phys. Chem. Lett.*, 2010, **1**, 540–543.
9 C. Shahar, D. Zbaida, L. Rapoport, H. Cohen, T. Bendikov, J. Tannous, F. Dassenoy and R. Tenne, *Langmuir*, 2010, **26**, 4409–4414.
10 H. Yang, S. Liu, J. Li, M. Li, G. Peng and G. Zou, *Nanotechnology*, 2006, **17**, 1512–1519.
11 L. Chang, H. Yang, W. Fu, N. Yang, J. Chen, M. Li, G. Zou and J. Li, *Mater. Res. Bull.*, 2006, **41**, 1242–1248.
12 N. Zink, J. Pansiot, J. Kieffer, H. A. Therese, M. Panthöfer, F. Rocker, U. Kolb and W. Tremel, *Chem. Mater.*, 2007, **19**, 6391–6400.
13 N. Zink, H. A. Therese, J. Pansiot, A. Yella, F. Banhart and W. Tremel, *Chem. Mater.*, 2008, **20**, 65–71.
14 A. Margolin, F. L. Deepak, R. Popovitz-Biro, M. Bar-Sadan, Y. Feldman and R. Tenne, *Nanotechnology*, 2008, **19**, 095601.
15 X.-L. Li, J.-P. Ge and Y.-D. Li, *Chem.–Eur. J.*, 2004, **10**, 6163–6171.
16 I. Wiesel, H. Arbel, A. Albu-Yaron, R. Popovitz-Biro, J. M. Gordon, D. Feuermann and R. Tenne, *Nano Res.*, 2009, **2**, 416–424.
17 M. Remskar, M. Virsek and A. Jesih, *Nano Lett.*, 2008, **8**, 76–80.
18 M. Bar-Sadan, S. G. Wolf and L. Houben, *Nanoscale*, 2010, **2**, 423–428.
19 HREM Research Inc., http://www.hremresearch.com.
20 *Materials Studio 4.0*, Accelrys Inc., San Diego, CA, 2003.
21 K. Ishizuka, *Ultramicroscopy*, 2001, **90**, 71–83.
22 S. Jeon and K. Yong, *Chem. Commun.*, 2009, 7042–7044.
23 G. Berhault, A. Mehta, A. C. Pavel, J. Yang, L. Rendon, M. Jose-Yacaman, L. C. Araiza, A. D. Moller and R. R. Chianelli, *J. Catal.*, 2001, **198**, 9–19.
24 G. Berhault, M. P. De la Rosa, A. Mehta, M. José-Yácaman and R. R. Chianelli, *Appl. Catal., A*, 2008, **345**, 80–88.
25 M. P. De la Rosa, S. Texier, G. Berhault, G. Camacho, M. José Yácaman, A. Mehta, S. Fuentes, A. Montoya, F. Murrieta and R. R. Chianelli, *J. Catal.*, 2004, **225**, 288–299.
26 P. D. Nellist and S. J. Pennycook, *Science*, 1996, **274**, 413–415.

27 S. J. Pennycook, *Ultramicroscopy*, 1989, **30**, 58–69.
28 K. van Benthem and S. J. Pennycook, *Appl. Phys. A: Mater. Sci. Process.*, 2009, **96**, 161–169.
29 Z. Y. Li, J. Yuan, Y. Chen, R. E. Palmer and J. P. Wilcoxon, *Appl. Phys. Lett.*, 2005, **87**, 243103.
30 D. Ferrer, A. Torres-Castro, X. Gao, S. Sepulveda-Guzman, U. Ortiz-Mendez and M. Jose-Yacaman, *Nano Lett.*, 2007, **7**, 1701–1705.
31 D. Ferrer, D. A. Blom, L. F. Allard, S. Mejía-Rosales, E. Perez-Tijerina and M. Jose-Yacaman, *J. Mater. Chem.*, 2008, **18**, 2442–2446.
32 A. N. Enyashin, M. Bar-Sadan, J. Sloan, L. Houben and G. Seifert, *Chem. Mater.*, 2009, **21**, 5627–5636.
33 F. L. Deepak, A. Mayoral, A. J. Steveson, S. Mejıa-Rosales, D. A. Blom and M. Jose-Yacaman, *Nanoscale*, 2010, **2**, 2286–2293.
34 A. Albu-Yaron, M. Levy, R. Tenne, R. Popovitz-Biro, M. Weidenbach, M. Bar-Sadan, L. Houben, A. N. Enyashin, G. Seifert, D. Feuermann, E. A. Katz and J. M. Gordon, *Angew. Chem., Int. Ed.*, 2011, **50**, 1–6.
35 H.-L. Tsai, J. Heising, J. L. Schindler, C. R. Kannewurf and M. G. Kanatzidis, *Chem. Mater.*, 1997, **9**, 879–882.

